Bioactive Materials 14 (2022) 302–312

Contents lists available at ScienceDirect

Bioactive Materials

journal homepage: www.keaipublishing.com/en/journals/bioactive-materials

A dual-gelling poly(*N*-isopropylacrylamide)-based ink and thermoreversible poloxamer support bath for high-resolution bioprinting

Adam M. Navara, Yu Seon Kim, Yilan Xu, Christopher L. Crafton, Mani Diba, Jason L. Guo, Antonios G. Mikos *

Department of Bioengineering, Rice University, 6500 Main Street, Houston, TX, 77030, USA

ARTICLE INFO

Keywords:
Bioprinting
Thermogelling macromer
Tissue engineering
Printability

ABSTRACT

Extrusion bioprinting is a popular method for fabricating tissue engineering scaffolds because of its potential to rapidly produce complex, bioactive or cell-laden scaffolds. However, due to the relatively high viscosity required to maintain shape fidelity during printing, many extrusion-based inks lack the ability to achieve precise structures at scales lower than hundreds of micrometers. In this work, we present a novel poly(*N*-isopropylacrylamide) (PNIPAAm)-based ink and poloxamer support bath system that produces precise, multilayered structures on the tens of micrometers scale. The support bath maintains the structure of the ink in a hydrated, heated environment ideal for cell culture, while the ink undergoes rapid thermogelation followed by a spontaneous covalent crosslinking reaction. Through the combination of the PNIPAAm-based ink and poloxamer bath, this system was able to produce hydrogel scaffolds with uniform fibers possessing diameters tunable from 80 to 200 μm. A framework of relationships between several important printing factors involved in maintaining support and thermogelation was also elucidated. As a whole, this work demonstrates the ability to produce precise, acellular and cell-laden PNIPAAm-based scaffolds at high-resolution and contributes to the growing body of research surrounding the printability of extrusion-based bioinks with support baths.

1. Introduction

Bioprinting is a rapidly growing method for biomaterial fabrication due to its potential in using cell-laden or bioactive materials as building blocks to create architecturally complex constructs that more closely recapitulate native tissue [1–3]. The development of innovative and affordable hardware has triggered a wave of material design and research focused on creating new inks that take full advantage of the hardware's capabilities. In particular, the design of hydrogels and other polymeric materials, often referred to as "inks" in the context of 3D printing, has seen increased discussion in the literature due to their suitability in culturing cells for implantation, as well as the room for improvement regarding resolution and cytocompatibility [4–7]. For example, extrusion printing is one methodology which presents the possibility of rapidly fabricating clinically-sized cell-laden constructs using hydrogel materials with a well-documented history of supporting cell growth and differentiation [8,9]. However, this approach can be limited by the fairly high viscosity of many materials used in extrusion printing (10s–1000s Pa*s) [10–13] which limits the size of the nozzle that can be used and thus the overall printing resolution. Recent innovations that circumvent this issue include dual-gelling inks that rely on a rapid, physical gelation to stabilize their structure followed by a more permanent secondary crosslinking [14–17], as well as support baths that hold low viscosity inks in place until a secondary stabilization method, usually ultraviolet-induced crosslinking, can take place [18–23]. Typically these baths are composed of gelatin microparticles [18,20], however recent publications have also made use of agarose [21], alginate [22], and a poloxamer/alginate mix [23].

Our laboratory has previously developed a poly(*N*-isopropylacrylamide)-based dual-gelling macromer that has been demonstrated to be a promising material for osteochondral tissue engineering applications, in part because of the high number of hydrophobic regions conducive to mineralization present in this PNIPAAm-based hydrogel relative to other hydrogel materials [24–28] (Figure S1). This macromer, hereafter referred to as "TGM" for thermogelling macromer, consists of primarily poly(*N*-isopropylacrylamide) (PNIPAAm), which gives

Peer review under responsibility of KeAi Communications Co., Ltd.
* Corresponding author. Department of Bioengineering, Rice University, 6500 Main St, Houston, TX, 77030, USA.
E-mail address: mikos@rice.edu (A.G. Mikos).

https://doi.org/10.1016/j.bioactmat.2021.11.016
Received 9 September 2021; Received in revised form 25 October 2021; Accepted 10 November 2021
Available online 19 November 2021

the material its thermogelling and relatively hydrophobic nature. Due to the syneresis frequently undergone by PNIPAAm materials, as well as the thermoreversible nature of the PNIPAAm and the relatively low mechanical properties of gels that solely rely upon thermal gelation, PNIPAAm is copolymerized with glycidyl methacrylate (GMA) to provide an epoxy ring for epoxy-amine crosslinking. Additionally, since PNIPAAm is not biodegradable, (*R*)-α-acryloyloxy-β,β-dimethyl-γ-butyrolactone (DBA) is copolymerized to add a lactone ring that will hydrolyze over time and increase the hydrophilicity of the material. Since the lower critical solution temperature (LCST) of TGM is dependent on the overall hydrophobicity of the material, the LCST will slowly increase over time until the polymer is no longer thermally gelled at physiological temperature, resulting in eventual degradation of the macromer. Finally, acrylic acid is included to offset the effects on the LCST of the hydrophobic GMA and DBA components and maintain workability at room temperature. A poly(amidoamine) (PAMAM) crosslinker is used to crosslink the polymer network via an epoxy-amine reaction with the GMA component (Figure S2), leading to prevention of syneresis, mechanical strengthening, and maintenance of the polymeric network following the hydrolysis of the DBA components. The amide bonds within the PAMAM will eventually hydrolyze as well and then lead to degradation of the hydrogel [24,25].

Due to its thermogelling nature, TGM was previously investigated for use as an injectable material, remaining a liquid at room temperature but solidifying when exposed to physiological temperatures above its LCST. However, during injection it is difficult to create heterogeneous scaffolds other than layered constructs. For this reason, we were interested in evaluating the success of TGM as a bioink, leveraging its thermogelling properties to rapidly resolve the relatively low viscosity material into organized fibers before chemical crosslinking occurs with the incorporated PAMAM. Due to this low viscosity, a support bath was necessary to maintain the fidelity of extruded fibers while thermal gelation took place (Figure S3). This thermal gelation needed to take place above the LCST of the TGM, which precluded the use of gelatin as a support material, since gelatin would solubilize at these temperatures. We also wanted to maintain the possibility of solubilizing the bath through reversing its thermogelation, as we believed this could be beneficial in releasing large constructs quickly from the support material. For these reasons, we adopted a poloxamer, Synperonic® F-108, as our support material for this work. Synperonic® baths are simple to prepare, as the material only needs to be dissolved in a solvent at its working concentration before use. This material also possesses the added advantage of maintaining the printed constructs in a hydrated environment at physiological temperatures, making it ideal for cell printing conditions with various types of inks. Finally, the bath conducts heat effectively to all layers of the printed TGM scaffolds, which would be challenging in an open-air environment due to the lower heat capacity of air, resulting in non-gelled upper layers.

To this end, we sought to assess the potential of TGM and Synperonic® F-108 as a bioink and biosupport bath, respectively. We first examined the rheological characteristics of both materials, to acquire an understanding of the properties that will affect their behavior during printing and to compare to previous ink-bath systems. We then studied the printability of the system through two factorial experiments meant to look at the interaction between the ink and the bath as well as the interaction between the ink and the nozzle diameter. Finally, we sought to evaluate the potential for cell printing with this system through a preliminary cell printing study with a representative group from the printability studies.

2. Materials and methods

2.1. Materials

N-isopropylacrylamide (NIPAAm), glycidyl methacrylate (GMA), (*R*)-α-acryloyloxy-β,β-dimethyl-γ-butyrolactone (DBA), acrylic acid (AA), 2,2′-azobis(2-methylpropionitrile) (AIBN), *N*,*N*′-methylenebis (acrylamide) (MBA), piperazine, Synperonic® F-108, sodium bicarbonate, D-(+)-glucose, L-glutamine, sodium pyruvate, 1,4-dioxane, acetone, and rhodamine B were purchased from MilliporeSigma (St. Louis, MO). Diethyl ether and live/dead assay were purchased from Fisher Scientific (Waltham, MA). L929 mouse fibroblasts were purchased from American Type Culture Collection (Manassas, VA). Low-glucose Dulbecco's modified Eagle medium (DMEM), DMEM with no glucose, glutamine, or phenol red, and antibiotic-antimycotic were purchased from Gibco (Thermo Fisher Scientific, Waltham, MA). Fetal bovine serum was purchased from Gemini Bioproducts (West Sacramento, CA).

2.2. Synthesis of thermogelling macromer

The four-part TGM was synthesized according to previous protocols [25]. NIPAAm, GMA, DBA, and AA were added to nitrogen-purged dioxane at a molar feed ratio of 86.5:7.5:3.5:2.5 respectively, along with 0.1% w/v AIBN, and reacted at 65 °C for 16 h. The solvent was then removed with rotary evaporation, and the remaining reaction product was redissolved in acetone and twice purified via dropwise ether precipitation and filtration. The resulting product was then stored under vacuum until further use. The average molar ratio of the comonomers in the synthesized TGM product was confirmed with a combination of ^{1}H NMR (600 MHz Bruker NEO Digital NMR Spectrometer, Bruker, Billerica, MA) and acid-base titration to be 87.9:6.5:1.9:3.7. The final number-average molecular weight (M_n), weight-average molecular weight (M_w), and polydispersity index (PDI) of purified TGM were measured by an ACQUITY advanced polymer chromatography (APC) system (Waters Corporation, Milford, MA) with reference to polystyrene standards to be 19849 ± 1614 Da, 54446 ± 296 Da and 2.76 ± 0.23, respectively. The average LCST of the TGM was determined via differential scanning calorimetry (DSC250, TA Instruments, New Castle, DE) to have an onset of 19.9 ± 0.7 °C and a peak of 25.5 ± 1.0 °C.

2.3. Synthesis of poly(amidoamine) crosslinker

The PAMAM crosslinker was synthesized according to previous protocols [24,25]. MBA and piperazine were added to nitrogen-purged ultrapure water at a molar ratio of 3:4 and allowed to react at 30 °C for 48 h. The reaction mixture was then purified via acetone precipitation and filtered. Successful synthesis was confirmed via ^{1}H NMR as well as through observation of appropriately sized peak separation in MALDI-ToF mass spectrometry (AutoFlex Speed MALDI ToF, Bruker, Billerica, MA). The M_n of the PAMAM crosslinker was estimated according to prior methods [24] to be 1776 ± 319 Da.

2.4. Preparation of TGM inks and Synperonic® baths

TGM inks were prepared by dissolving TGM and PAMAM in phosphate buffered saline (PBS) at twice their final concentration. The TGM and PAMAM solutions were kept separate and on ice until immediately before use due to the spontaneous nature of the reaction between the macromer and crosslinker and the thermosensitivity of the TGM. When ready, the TGM and PAMAM solutions were mixed at a 1:1 ratio to reach their final working concentrations. The mass ratio of TGM to PAMAM was kept at a constant 4:3 TGM:PAMAM, which was the ratio previously deemed most effective at eliminating syneresis of TGM gels [24]. This constant ratio resulted in inks with a final polymer content of 17.5% w/v (10% TGM, 7.5% PAMAM), 26.25% w/v (15% TGM, 11.25% PAMAM), and 35% w/v (20% TGM, 15% PAMAM).

Synperonic® baths were prepared by simply adding the Synperonic® F-108 to ultrapure water at either 25%, 30%, or 35% w/v and dissolved over night at 4 °C.

2.5. Rheological analysis of TGM inks and Synperonic® baths

Rheological properties of TGM inks and Synperonic® baths were assessed using a Discovery HR-1 hybrid rheometer (TA Instruments, New Castle, DE). Ink and bath viscosity at varying shear rates as well as bath moduli and bath yield stress were assessed using a 20 mm flat stainless steel geometry. Ink thermogelling behavior and bath recovery following cyclic high strains were assessed using a 40 mm flat stainless steel geometry with a solvent trap that was filled with water during the procedure. Ink and bath viscosity was measured with a shear rate ramp from 0.1 to 1000 s^{-1} at the printing temperature of 12.5 °C for the ink and 37 °C for the bath. Ink thermogelling behavior was assessed using oscillatory time sweeps at 1% strain and 1 Hz, maintaining the temperature at 12.5 °C for 300 s before ramping the temperature at a rate of 10 °C/min until reaching 37 °C and sampling for an additional 300 s. Bath storage modulus (G′) and loss modulus (G″) were assessed through oscillatory strain sweeps at 1 Hz over a strain range of 0.01%–1000%. Bath yield stress was assessed through an oscillatory stress ramp at 1 Hz over a range of stress from 1 to 1000 Pa. The yield stress was determined to be where lines fitted to the original plateau and the linear decrease in G' intersected. Finally, bath recovery was measured by 3.5 cycles of oscillatory time sweeps of 2 min of low strain (1%) followed by 2 min of high strain (1000%). Five samples were analyzed for each group in each procedure ($n = 5$).

2.6. Indentation analysis of TGM gels

TGM and PAMAM solutions were prepared according to procedures outlined in section 2.4. They were then mixed and pipetted into cylindrical Teflon molds with a 6 mm diameter and 2 mm height and incubated at 37 °C for 24 h. The resulting TGM hydrogels were removed from the molds and placed in excess PBS and allowed to swell for an additional 24 h. Atomic force microscopy (AFM) was conducted in the University of Texas Health Science Center AFM Core Facility using a BioScope2 TM Controller (Bruker, Billerica, MA). The acquisition of elastic measurements was performed with the Research NanoScope software version 7.30 (copyright Bruker). This system was integrated to a Nikon TE2000-E inverted optical microscope (Nikon Instruments, Melville, NY) to facilitate bright field observation. The elastic (Young's) modulus was measured on hydrated gels immersed in ultrapure water, capturing force curves from at least 8 randomly selected sites in each gel, using Novascan colloidal AFM probes. These probes consisted of a 5-μm diameter borosilicate glass particle attached to the edge of a silicon nitride V-shaped cantilever with a nominal spring constant of 0.24 N/m. The cantilever was calibrated for its laser sensitivity using the thermal oscillation method prior to each experiment. Indentation curves were captured using 4-μm ramp sizes, a scan rate of 0.5 Hz, and a trigger threshold with a maximum load of 10 nN. Young's modulus was calculated following the Hertz model (spherical indenter radius = 2.5 μm) with a Poisson's ratio of 0.45 (given to hydrogels), using the NanoScope Analysis software version 1.5 (Bruker). Five samples were tested for each group ($n = 5$).

2.7. Printing and assessment of TGM scaffolds

2.7.1. Printing procedure

TGM, PAMAM, and Synperonic® solutions were prepared as outlined in section 2.4, with the exception that a 0.1% w/v rhodamine B solution was added to the PAMAM solution at a 0.4% v/v ratio to aid in visualizing the ink during printing as well as fluorescently imaging the scaffolds for the printability assessment. A Cellink BIO X 3D printer (Cellink, Boston, MA) equipped with a temperature-controlled pneumatic printhead was used for all printing. Synperonic® baths were prepared in 12 well plates and heated to 37 °C, which was verified with a digital thermometer immediately before printing. Due to the spontaneous nature of the crosslinking reaction, TGM and PAMAM solutions were aliquoted out for replicate prints and were not mixed until immediately before printing. While the effect of the ongoing crosslinking reaction on printability was expected to be minimal, due to the slow kinetics of the reaction [24], all scaffolds compared during post-printing analysis were from similar timepoints following mixing of the macromer and crosslinker to avoid any variability due to different degrees of crosslinking. Once mixed, the inks were placed inside of a chilled cartridge and then into the temperature-controlled pneumatic printhead set to 12.5 °C. The inks were then extruded into the heated support bath into their desired pattern. During printing, the unused wells were covered with parafilm to minimize bath drying before use. A video of the inks during printing is available in the supplemental information (Video S1).

After all scaffolds were printed, the plate was covered and sealed and left to incubate at 37 °C for 2 h for covalent crosslinking to complete. The printed scaffolds were then removed via a spatula, still encased in excess bath for stability, before being placed in excess water at room temperature to wash away the remaining bath material. This procedure is outlined in Fig. 1.

2.7.2. Ink concentration vs. bath concentration study

Three ink concentrations (17.5%, 26.25%, 35% w/v) were assessed in combination with three bath concentrations (25%, 30%, 35% w/v) using two different nozzle sizes (27G, 32G). Layer height was kept at 0.15 mm for 27G groups and 0.05 mm for 32G groups. To maintain a constant ink:bath ratio, the infill density was kept at 25% for all groups. Additionally, the speed of the nozzle was kept at a constant 5 mm/s for all groups. The initial layer height was set to be only 25% of the actual layer height, to ensure that the nozzle would come into contact with the previous layer during printing. The dimensions of all scaffolds printed were 10 mm × 10 mm × the layer height multiplied by the number of layers.

The appropriate printing pressure for each group was determined to be the minimum pressure that would produce scaffolds which maintained their fidelity once removed from the support bath while also avoiding clogging the nozzle during printing. Appropriate scaffold fidelity was determined through printing four-layered scaffolds and scoring them either 0, 0.5, or 1.0 (Figure S4). The minimum pressure that could produce scaffolds with an average fidelity score over 0.5 ($n = 6$) was selected as the pressure for that group. Four-layered scaffolds were used for this metric, as they were deemed to be more relevant (due to the presence of more layers) than the two-layered scaffolds used for the other printability metrics. The selected printing pressures for each group are presented in Fig. 2.

Two-layered scaffolds were printed to assess fiber diameter, pore circularity, pore shape uniformity, and pore area uniformity, due to their unobstructed view of pore shape and size caused by successive layers in larger scaffolds. Fluorescent microscopic images of the scaffolds were acquired and analyzed using ImageJ software. Fiber diameter was determined by applying a random set of lines across an image and measuring the diameter at the intersection point of the fiber and line. Pore circularity was determined using the previously established Pr score metric [29] in which Pr is based upon the circularity of a perfect rectangle such that:

$$\mathrm{Pr} = \frac{Perimeter^2}{16 * Area}$$

where perimeter and area refer to the perimeter and area of the pore, and an ideal Pr score (perfectly rectangular) is equal to 1. As a measure of precision, the uniformity of the shapes of the pores was calculated using the relative standard deviation of the Pr score in a sample, such that:

$$Shape\ \ Uniformity = 1 - \left(\frac{\frac{\sigma_{Pr1}}{\mu_{Pr1}} + \frac{\sigma_{Pr2}}{\mu_{Pr2}}}{2}\right)$$

where σ_{Pr1} and μ_{Pr1} are the standard deviation and mean, respectively, of

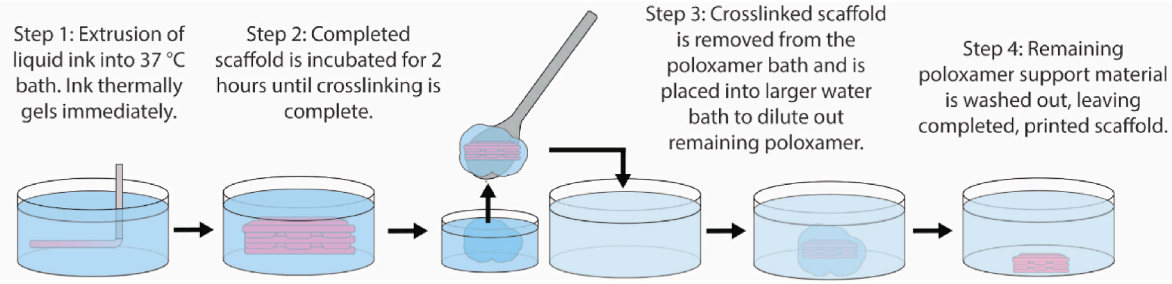

Fig. 1. Printing process. TGM ink is cooled down to 12.5 °C and then extruded into a Synperonic® F-108 support bath heated to 37 °C, where it immediately undergoes thermal gelation. It is then incubated for 2 h while covalent crosslinking completes before being removed and placed into excess water to wash away remaining bath material. Steps 1 and 2 are depicted at a smaller scale than steps 3 and 4.

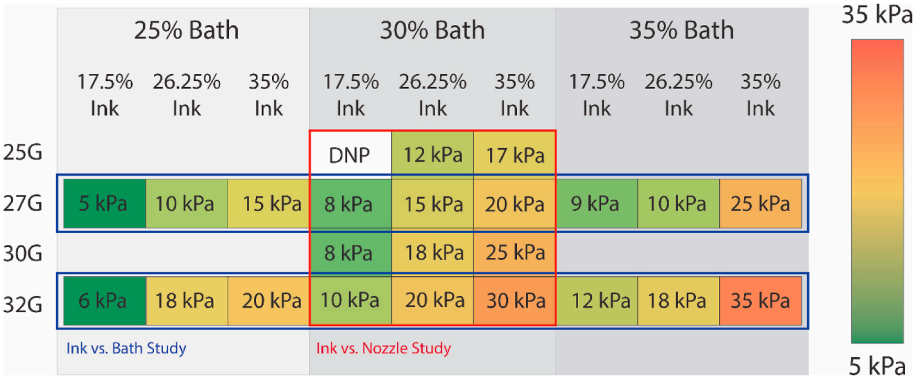

Fig. 2. Printing pressure used for each group in the two printability studies. Printing pressures were selected as the minimum pressure necessary to produce a four-layered scaffold with a fidelity score of at least 0.5. Fidelity score determined with $n = 6$ for all groups. DNP indicates that the group did not print at any pressure.

the Pr scores for type 1 pores and σ_{Pr2} and μ_{Pr2} are the standard deviation and mean, respectively, of the Pr scores for type 2 pores. Type 1 and type 2 refers to the handedness of the pores being analyzed. Due to the different directions of the nozzle, pores will acquire a handedness, being relatively identical to other pores in their column, but mirror images of the pores above and below (Figure S5). As such, the relative standard deviation of the Pr score was calculated for each of the two pore handedness, and then averaged for the final calculation of pore shape uniformity. Finally, a second measure of precision, pore area uniformity, was calculated by determining the relative standard deviation of the areas of the pores in a sample, regardless of handedness, such that:

$$Area\ \ Uniformity = 1 - \frac{\sigma_{Pore\ \ Area}}{\mu_{Pore\ \ Area}}$$

where $\sigma_{Pore\ \ Area}$ and $\mu_{Pore\ \ Area}$ are the standard deviation and the mean of the pore areas, respectively. Five scaffolds were analyzed for each of the experimental groups ($n = 5$).

2.7.3. Ink concentration vs. nozzle size study

Three ink concentrations (17.5%, 26.25%, 35%) were printed with four different nozzle sizes (25G, 27G, 30G, 32G) in a 30% Synperonic® bath. Layer height for the nozzles was maintained at 0.2 mm, 0.15 mm, 0.1 mm, and 0.05 mm for 25G, 27G, 30G, and 32G nozzles respectively. As in the previous printability study, infill density was kept at a constant 25% for all groups, nozzle speed was kept at 5 mm/s, and the first layer height was set at 25% of the expected layer height to ensure layer to layer contact. Appropriate printing pressures were again determined through the scaffold fidelity test using four-layered constructs (Fig. 2), while two-layered scaffolds were printed for fiber diameter, Pr score, shape uniformity, and area uniformity assessments, as outlined in section 2.7.2. Five scaffolds were analyzed for each of the experimental groups ($n = 5$). Groups that were already studied in section 2.7.2 (30% bath – 27G/32G) were not repeated, so the associated data is identical in both studies.

2.7.4. Large scaffold printing

In order to obtain a clearer perspective of the side view of the printed scaffolds and to demonstrate that this system can print constructs on a millimeter scale, a larger 10 mm × 10 mm × 5 mm scaffold was printed using the 35% TGM – 30% Synperonic® F-108 – 27G nozzle group. The printing procedure used was identical to the one outline in section 2.7.1 with the exception that the scaffold was printed in a glass Petri dish with a 100 mm diameter. With a layer height of 0.15 mm, the final construct consisted of 33 layers. After removal, the scaffold was imaged from a macroscopic, orthographic, and side view.

2.8. Cellular compatibility of TGM inks

2.8.1. Leachables assay

L929 fibroblasts were cultured in low-glucose DMEM with 10% v/v FBS and 1% v/v antibiotic-antimycotic, receiving new media every other day, until ready for study. All cells used in the study were passage 6 or less. TGM and PAMAM were sterilized via UV exposure for 6 h before preparing into 17.5%, 26.25%, and 35% TGM hydrogels as described in section 2.6. Following fabrication, the TGM hydrogels were then placed in serum-free L929 media at a gel surface area:media volume ratio of 3 cm^2:1 mL and incubated at 37 °C for 24 h. The leachables media was then removed, sterile filtered, and diluted, resulting in 1X, 10X, and 100X solutions. L929s were plated in 96 well plates at 10,000 cells/well and cultured for 24 h, reaching 80% confluency. They were then washed with PBS before adding 100 μL of either serum-free media or leachables media and incubated at 37 °C. At both 2 h and 24 h timepoints, the media was removed, the cells were washed three times with PBS, and then exposed to live/dead stain that was prepared according to the manufacturer's instructions. The plates were then

scanned with a FLx800 microplate fluorescence reader (Biotek, Winooski,VT) using 485/528 nm excitation/emission filter set to measure the live cell signal. Percent viability was determined by normalizing the experimental live signal to the positive control.

2.8.2. Printed cell viability study

L929 fibroblasts were cultured as described in section 2.8.1, until ready for printing. All cells used in the study were passage 4. A 26.25% TGM ink, 30% Synperonic® bath, and 27G nozzle were selected as the model group for the study, due to its printing success and median placement amongst the groups. TGM, PAMAM, and Synperonic® were sterilized via UV exposure for 6 h. TGM and PAMAM were then solubilized in L929 media while Synperonic® was solubilized in phenol red-free DMEM supplemented with 1000 mg/L D-(+)-glucose, 584 mg/L L-glutamine, 110 mg/L sodium pyruvate, 3.7 g/L sodium bicarbonate, 10% FBS, and 1% antibiotic-antimycotic. Phenol red was excluded in order to facilitate visibility of the fibers, which did contain phenol red, by the user during the printing process. Cells were passaged and resuspended to their working concentration before being placed on ice, in an effort to mitigate both temperature shock experienced by cells during mixing with the TGM as well as premature thermogelation of the TGM. Six aliquots separating the TGM and PAMAM were prepared to minimize the differences in degree of crosslinking, as discussed in section 2.7.1. Immediately before printing, the cells were mechanically mixed with TGM and PAMAM to a final concentration of 10,000,000 cells/mL. Once mixed, the cells were printed into both four- and two-layered scaffolds, one for each aliquot, as described in section 2.7.1, at 15 kPa. Both four-layered and two-layered scaffolds were printed as an internal quality control metric to assess appropriate printing success. Once printed, the scaffolds were incubated within the baths at 37 °C for 2 h, before being removed and placed in excess L929 media and stored again in an incubator at 37 °C. The removal of the scaffolds from the bath, 2 h after printing, was selected as time 0 for viability purposes. The baths were not fully washed away until 3 h after removal, at which point half of the scaffolds were washed three times with PBS and stained with live/dead for viability assessment via fluorescent imaging. At 24 h, the process was repeated with the remaining scaffolds. Viability was then determined using ImageJ software to count all particles with an area of 50–800 μm^2 in both the green (live) and red (dead) channels. Both four-layered and two-layered scaffolds were used in viability assessments, as viability was determined to be independent of number of layers present.

2.9. Statistics

Experimental groups in the printability studies and leachables assay were compared with two-way analysis of variance (ANOVA) followed by Tukey's honest significant difference (HSD) ($p < 0.05$). Values presented in text and figures are mean ± standard deviation unless otherwise stated.

3. Results and discussion

3.1. Rheological analysis of TGM inks and Synperonic® bath

The rheological properties of bioinks are the primary determinant of their printability, to the point where they have been used as a metric for predicting printing success [10]. Viscosities of the TGM inks were determined to be lower than 1 Pa*s for all ink concentrations studied (Fig. 3A), which falls several orders of magnitude below the range thought to be necessary for support-free extrusion printing [10] and reiterates the necessity for a support bath to maintain the structural fidelity of printed fibers. The TGM inks also demonstrated shear-thinning properties, which is common among polymer solutions due to chain disentanglement and advantageous for extrusion printing [30]. The Synperonic® bath was also found to be shear-thinning at all concentrations, indicating that the nozzle will be minimally disrupted during its movement through the bath (Figure S6). Next, the thermogelling behavior of the TGM inks was assessed to examine the pre- and

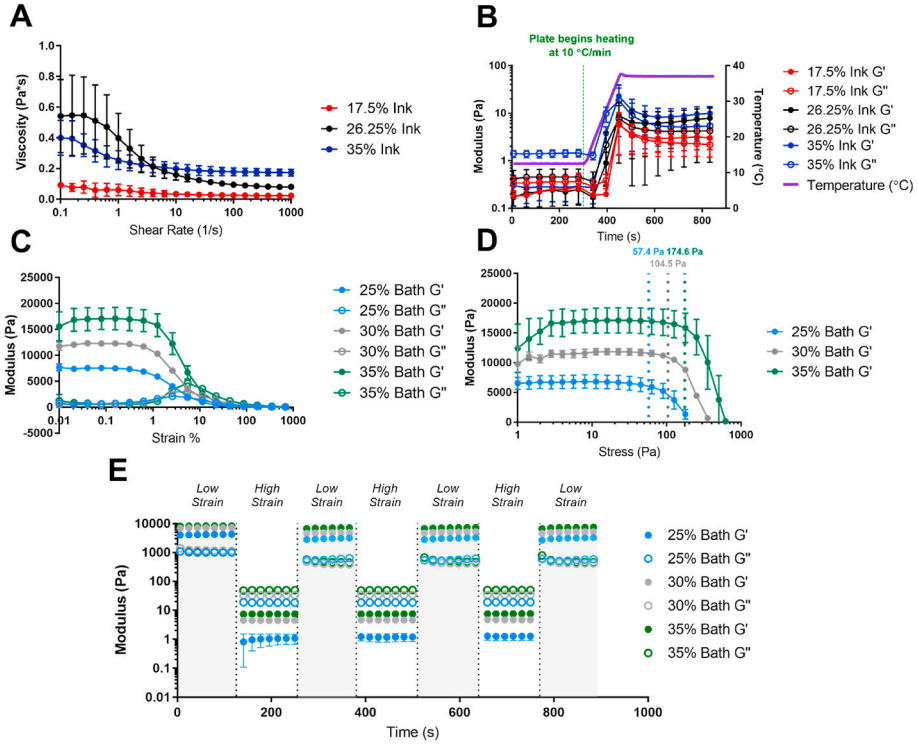

Fig. 3. Rheological assessment of TGM inks and Synperonic® baths. (A) Shear rate dependence of TGM ink viscosity. (B) G′ and G″ of TGM inks at 12.5 °C, during a 10 °C/min ramp, and at 37 °C. (C) Strain-dependent behavior of Synperonic® bath G′ and G". (D) Stress-dependent G′ of Synperonic® baths with calculated yield stress. (E) Strain recovery of Synperonic® baths at alternating strains of 1% and 1000%. $n = 5$ for all groups.

post-gelation viscoelastic behavior of the inks, as well as their responsiveness to the temperature change (Fig. 3B). All three ink concentrations showed a viscous-dominant phase (G" > G′) at 12.5 °C and an elastic-dominant phase (G' > G") at 37 °C. In addition, all three inks rapidly gelled within a minute when exposed to the temperature ramp. The rate of this gelation and its starting point were identical for all three ink concentrations, demonstrating the independence of LCST and thermogelation rate from polymer concentration.

The strain-dependent storage and loss moduli of the three bath concentrations were measured to determine their elasticity (Fig. 3C), which affects how stable the bath is during the printing process. At low strains (0.01%–1%), the baths had a G′ near 7.5 kPa, 13 kPa, and 17 kPa for 25%, 30%, and 35% concentrations respectively, before yielding around 1% strain. These G′ values are higher than other materials used for support bath extrusion printing [18,20], although any changes in support offered from such differences would need to be studied in greater detail. In addition, the yield stress was measured via a stress sweep. Yield stress serves as a metric for the bath's ability to self-heal, as it is the yield stress that needs to be overcome by hydrostatic forces in order for the crevices left by the path of the nozzle to collapse. Yield stress also represents the resistance the bath offers to ink extrusion. The yield stress was calculated as the intersection point of lines fitted to the pre-yield plateau region of the curve and to the descending linear post-yield portion, and was determined to be 57.4 Pa, 104.5 Pa, and 174.6 Pa for 25%, 30%, and 35% Synperonic® baths, respectively (Fig. 3D). Finally, the recovery of each bath following oscillating magnitudes of strain was measured to determine how well the baths maintained their mechanical properties following repeated exposure to high stress, which occurs when the printing nozzle moves through the bath repeatedly (Fig. 3E). The G′ value following high strain was found to be consistent and independent of the number of cycles, and was found to be 76.0%, 69.8%, and 87.9% of the original low strain G′ measurement for the 25%, 30%, and 35% baths respectively. Despite the reduction, these values represent a maintenance of a G′ on the order of several kPa, which is enough to maintain support for the printed structures following multiple passes of the nozzle.

3.2. Indentation analysis of TGM gels

Prior work assessing the mechanical properties of printed and bulk hydrogels of identical materials found no significant difference in elastic modulus based on fabrication method [31]. Therefore, due to the difficulty in securing printed fibers for AFM analysis, because of their small size and an inability to print them directly onto a substrate, AFM indentation of bulk TGM hydrogels was used to approximate the stiffness of the cellular microenvironment within printed TGM fibers. The elastic modulus of each group was measured to be 9.5 ± 3.4 kPa, 11.2 ± 4.2 kPa, and 12.0 ± 4.8 kPa for 17.5%, 26.25%, and 35% w/v bioinks, respectively (Figure S7). When compared to previously studied thermogelling systems, these values are an order of magnitude higher [31–33] likely due to the additional covalent crosslinking via PAMAM. This increase in elastic modulus may be beneficial to the structural integrity of printed scaffolds and culture of encapsulated cells, aiding in the success of TGM inks in tissue engineering applications.

3.3. Printability of TGM inks with Synperonic® support bath

3.3.1. Effect of ink-bath relationship on printability

To study the effects of ink concentration and bath concentration on printing outcomes, as well as the relationship between the two, a factorial study was conducted using a range of ink concentrations (17.5%, 26.25%, 35%) and bath concentrations (25%, 30%, 35%). Two nozzle sizes (27G and 32G) were also selected, since the nozzle size determines the total area of the interface between the ink and the bath, and we hypothesized the exchange of water between the two to potentially affect printing outcomes. The fidelity of four-layered scaffolds (pictured on the left in Fig. 4A and B) was used to assess the appropriateness of the printing conditions, particularly the pressure, before proceeding to printability studies using two-layered scaffolds (pictured on the right of Fig. 4A and B). Four-layered scaffolds were included for a fidelity pre-test because two-layered scaffolds are not representative of the larger constructs that the TGM inks would likely be scaled to in any future applications. However, two-layered scaffolds were necessary for printability analysis, since additional layers beyond the first two tended to obstruct view of the pores. Analysis of the pores was selected as a primary component of printability in part because of the importance of pore size and porosity in fabricating constructs for tissue engineering [34]. As such, an important feature of bioprinted tissue engineering constructs is a predictable and uniform pore structure. In addition to analysis of pore shape and size, fiber diameter was used as a metric for overall resolution of the system.

Amongst the 27G groups, most groups had a mean fiber diameter within 150 μm and 200 μm (Fig. 4C), which was in part due to the 150 μm layer height established for 27G groups, as fibers with a mean diameter smaller than the layer height would likely fail the four-layer fidelity test. These diameters are smaller than the inner diameter of a 27G nozzle (inner diameter = 210 μm). We hypothesize that this may be due to thermally gelled ink building up along the inner wall of the nozzle, resulting in a restricted diameter. It may also be due to the nozzle stretching out deposited ink, although the diameter tended to remain quite constant along the length of a fiber, absent of any necking we might expect to occur during fiber stretching. Additionally, the moderately-sized standard deviation amongst observed fiber diameters of the same ink, bath, and printing pressure may also point towards an inner lining of gelled material, which would likely be fairly inconsistent in its thickness. While PNIPAAm-based materials do undergo syneresis, previous work investigating TGM gels found that syneresis could be effectively eliminated when combined with the appropriate amount of PAMAM crosslinker [24], so we think it is unlikely that this is the cause. Additionally, at pressures where nozzle clogging occurred, gradual narrowing of the fiber diameter was observed preceding thermally gelled ink clogging the nozzle, which would indicate that the thermal gelation of the ink along the walls of the nozzle can cause some channel narrowing while still allowing ink to extrude from the nozzle.

The Pr scores were not statistically significant amongst any of the 27G groups (Fig. 4D), with all groups having a mean Pr score above the ideal 1.0. This is expected, due to the slight deformation of the pores by the nozzle as it comes into contact with the prior layer, and is a necessary accommodation to ensure that the layers come into contact with each other since they are suspended in the support gel. The shape (Fig. 4E) and area uniformity (Fig. 4F) also remained fairly consistent amongst all 27G groups, with the only noticeable trend being a slightly significant decrease in the area uniformity for some 17.5% groups, which we hypothesized may have been due to dilution of the support bath from the release of water in the much less concentrated ink. This hypothesis was also supported by qualitative observations in the loss of overall construct structure among four-layered prints, as depicted by the macroscopic images of the 17.5% ink scaffolds in Fig. 4A and B.

Amongst the 32G groups, most had a mean fiber diameter within 50 μm and 100 μm (Fig. 4G). A trend can be observed of significantly higher Pr scores amongst 35% ink groups (Fig. 4H), which was also accompanied by significantly lower pore shape uniformity (Fig. 4I) and pore area uniformity (Fig. 4J). This trend may be a result of the relatively higher viscosity at high shear, present during printing, which would cause lower flow rates and an increase in dragging of printed fibers, deforming the resulting pores. In addition, the 17.5% ink again saw lower values in area uniformity at low bath concentrations, but not medium or high bath concentrations, further supporting the idea that osmotic transfer from the ink to the surrounding bath could be diluting the lowest concentration of baths to the point where they lose the ability to adequately support printing.

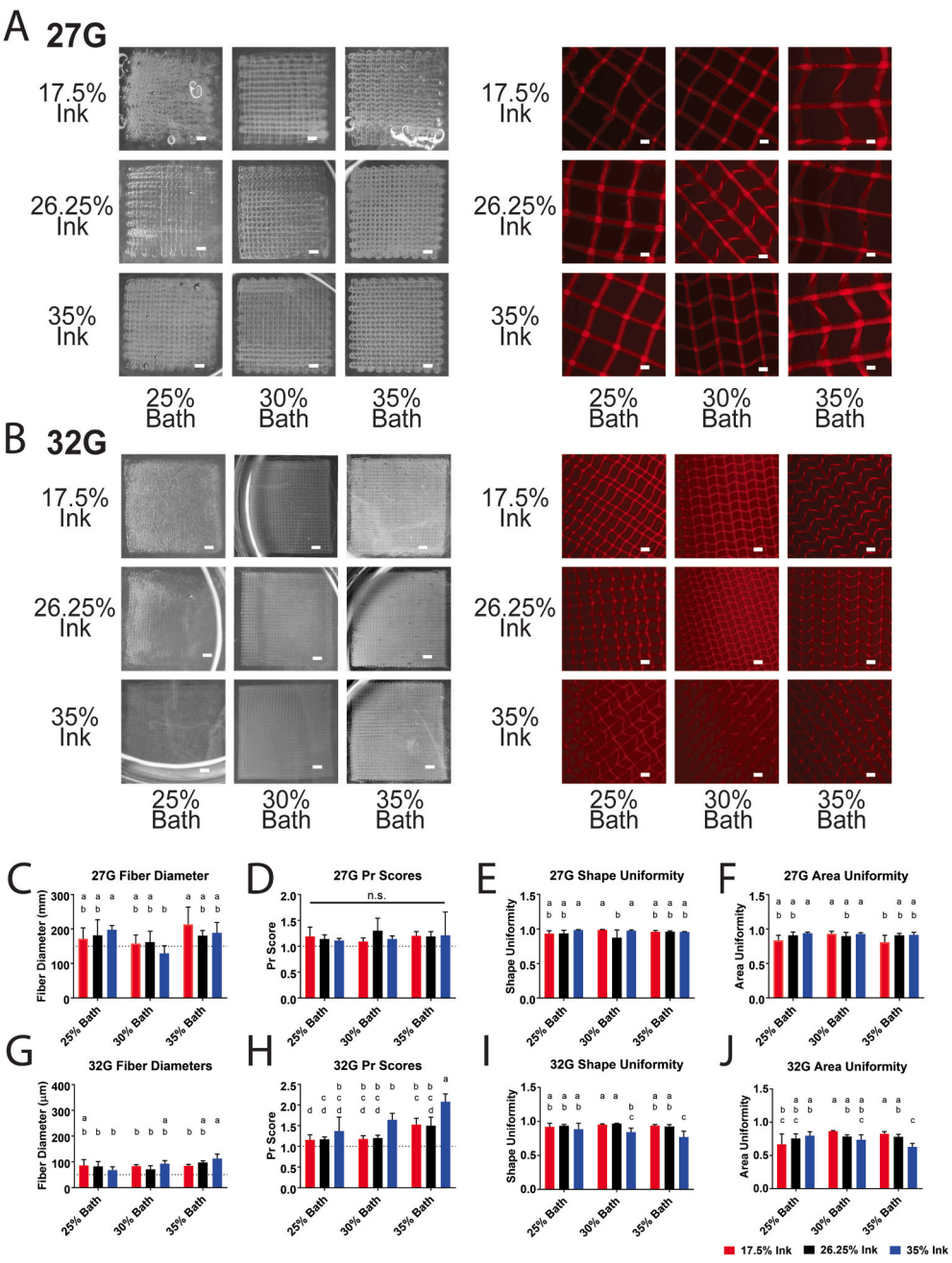

Fig. 4. Printability of TGM inks in different bath concentrations. (A–B) Macroscopic images of four-layered scaffolds (left) and microscopic images of two-layered scaffolds (right) printed with 27G (A) and 32G (B) nozzles. (C–F) Fiber diameter, Pr score, shape uniformity, and area uniformity of ink and bath combinations printed with a 27G nozzle. (G–J) Fiber diameter, Pr score, shape uniformity, and area uniformity of ink and bath combinations printed with a 32G nozzle. Groups with a shared letter are not significantly different from each other. Images were selected as closest to mean in fiber diameter and Pr score. Scale bars in macroscopic images are equal to 1 mm. Scale bars in microscopic images are equal to 250 μm. Dotted lines on graphs represent (C,G) layer height for that nozzle size and (D,H) ideal Pr score of 1.0. Significance was determined as $p < 0.05$. $n = 5$ for all groups.

3.3.2. *Effect of ink-nozzle relationship on printability*

While the study above focused on the relationship between the ink concentration and the bath concentration, a second printability study was conducted to study the combinatorial effects of the ink concentration and the nozzle diameter. This relationship is largely dominated by the shear forces present and any changes in printing pressure and flow rate as a result. Four nozzle diameters (25G, 27G, 30G, and 32G) were studied in combination with the same three ink concentrations, at a single bath concentration, 30%, which was selected as it was deemed the most successful of the baths in the previous study. As before, four-layered scaffolds (Fig. 5A, left) were printed to determine the printing pressure before two-layered scaffolds (Fig. 5A, right) were printed for printability assessment. No printing pressure was able to produce a consistently printed scaffold for the 17.5% ink – 25G nozzle group, due to consistent nozzle clogging at low pressures and significant over-extrusion at higher pressures. In general, all combinations of ink concentration and nozzle size were able to consistently print fibers with a diameter near the target layer height (Fig. 5B) with the possible exception of the 32G groups, which ran high, possibly because the smaller nature of the fibers made guaranteeing consistent layer adhesion and stability difficult. The Pr scores (Fig. 5C) and shape uniformity (Fig. 5D) showed no significant trend, apart from the outlier of the 32G – 35% ink group, indicating that as a whole, the combination of nozzle gauge and ink concentration had little effect on printing outcomes. Finally, the area uniformity (Fig. 5E) remained consistent with exception of the 32G groups, which showed a significant decrease. This decrease for the 32G groups is possibly due to the smaller nature of the fibers leading to easier deformation from the movement of the nozzle. However, it should also be noted that since area uniformity is relative to area size, a similarly sized dislocation of fibers will affect smaller pores to a greater extent, so the smaller nozzle size groups will be biased towards having a lower area uniformity. On the whole, the data presented in this study represents the ability for TGM inks in a 30% Synperonic® bath to be printed precisely and consistently at high resolutions and a

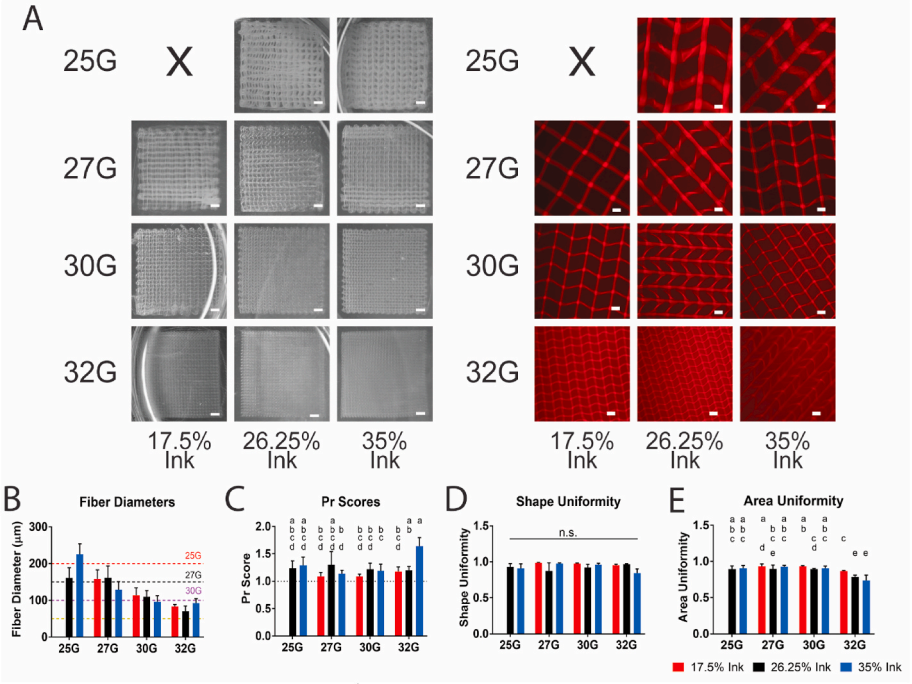

Fig. 5. Printability of TGM inks in a 30% Synperonic® bath with different nozzle sizes. (A) Macroscopic images of four-layered scaffolds (left) and microscopic images of two-layered scaffolds (right). (B–E) Fiber diameter, Pr score, shape uniformity, and area uniformity of TGM inks with different nozzle sizes. Groups with a shared letter are not significantly different from each other. Images were selected as closest to the mean of fiber diameter and Pr score. Scale bars in macroscopic images are equal to 1 mm. Scale bars in microscopic images are equal to 250 µm. Dotted lines on graphs represent (B) layer height for nozzle size and (C) ideal Pr score of 1.0. Significance was determined as $p < 0.05$. $n = 5$ for all groups. Images and data from groups also present in Fig. 5 are displayed here identically.

variety of sizes.

A reflection on the data from both studies reveals a complex web of factors that interact with one another to affect printability outcomes (Fig. 6). For example, quantitative and qualitative analyses of the relationship between ink concentration and bath concentration reveal a combinatorial effect on printability outcomes, which we believe is likely due to osmotic flow between the two destabilizing less concentrated baths, as seen in the 17.5% ink – 25% bath groups. Additionally, we observed that inks with higher concentrations would often have lower pore uniformity scores, especially at smaller nozzle sizes, likely due to their higher viscosity at higher shear. It should be noted as well that both the bath and ink temperature will certainly have an effect, due to the reliance on thermogelation of the system, although these two variables were held constant in the current studies.

3.3.3. *Large scaffold printing*

A 10 mm × 10 mm × 5 mm (33-layer) scaffold was also printed to allow for clearer visualization of the side profile of a printed TGM scaffold and to confirm the printing method could be scaled up to a larger vertical scale. A 35% TGM scaffold was successfully printed in a 30% Synperonic® bath using a 27G nozzle. The scaffold maintained comparable print quality throughout the 33 layers as to that of the smaller scaffolds in the printability studies (Figure S8, Video S2). This included both vertical and horizontal organization, and maintenance of overall construct porosity. This data indicates that this printing system can be effectively scaled up to address clinically-sized tissue defects while still maintaining uniform scaffold organization and high-resolution of printed fibers.

3.4. *Cellular viability within printed TGM scaffolds*

3.4.1. *Leachables assay*

To evaluate the presence of any potentially cytotoxic leachables material from the TGM inks, such as unreacted PAMAM crosslinker or oligomeric components, a leachables assay was conducted. After 2 h and 24 h, no significant change in viability was observed between the experimental groups and the positive control (Fig. 7A).

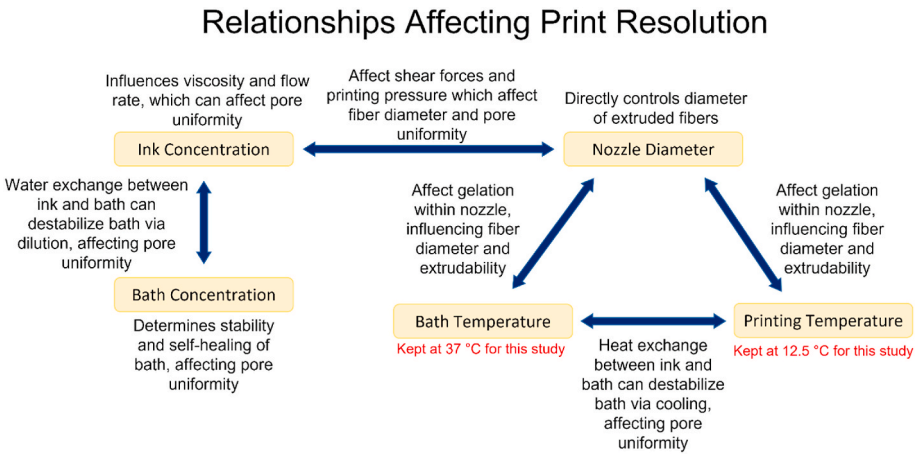

Fig. 6. Summary of the relationships between the factors during printing and how they affect printability outcomes.

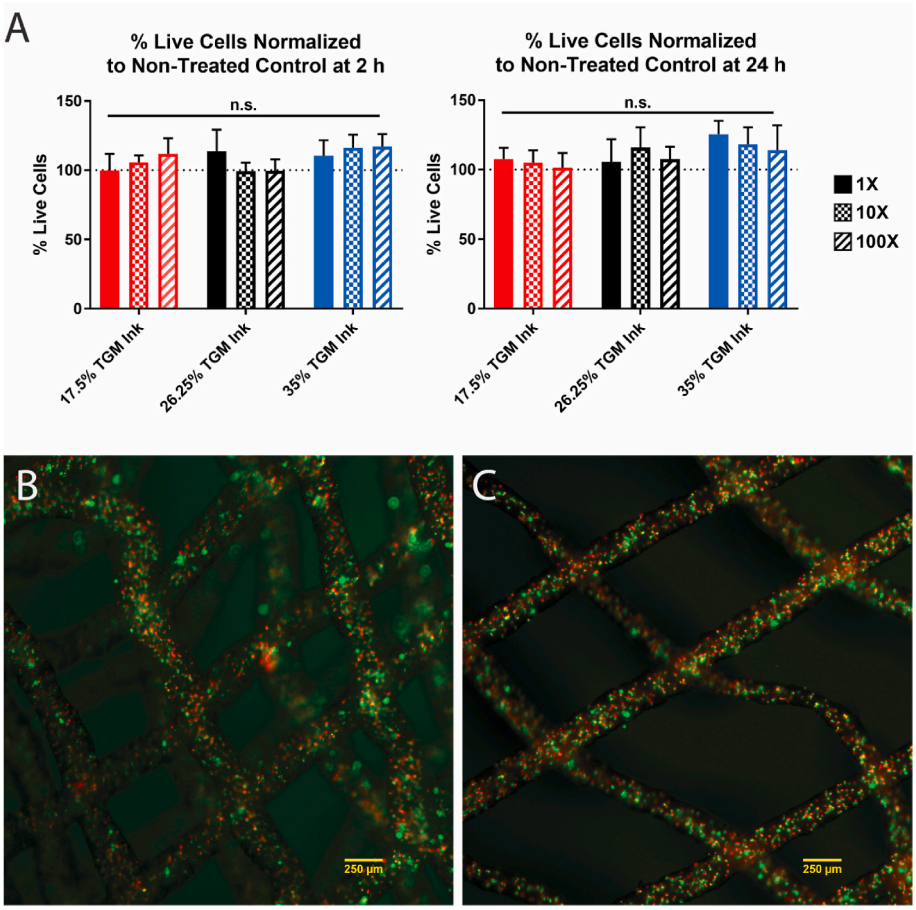

Fig. 7. Cellular compatibility of TGM inks. (A) 2 h and 24 h cell viability after exposure to TGM leachables media normalized to a live control group. (B) Four-layered scaffold with encapsulated L929s stained for live (green) and dead (red) cells at 3 h timepoint. (C) Two-layered scaffold with encapsulated L929s stained for live (green) and dead (red) cells at 24 h timepoint. Scale bars equal to 250 µm. $n = 4$ for all groups.

3.4.2. Printed cell viability study

Due to the low printing temperatures and rapid temperature change involved in the TGM printing procedure, we wanted to verify that cell viability could be maintained following cell printing with TGM inks. To this end, a pilot study using a single representative group from the prior printability studies was conducted. The 26.25% ink, 30% bath, 27G nozzle group was selected due to its relative printing success and median values. Both the TGM ink and the Synperonic® bath were solubilized in media to facilitate cell viability during and immediately following printing. L929s were added to the ink at 10,000,000 cells/mL and printed at 12.5 °C and 15 kPa into support baths heated to 37 °C. After printing, the scaffolds were then incubated for 2 h at 37 °C until cross-linking was complete and then removed and placed into excess L929 media and placed back into an incubator. The remaining bath took 3 h to wash away due to being stored in an environment above its LCST, and at the point the first groups of scaffolds were washed with PBS, stained with live/dead, and imaged (Fig. 7B).

Quantification of live and dead cells was done in ImageJ and the 3 h viability was found to be 43.6 ± 3.2% viable. This process was repeated with the remaining scaffolds at 24 h (Fig. 7C) and the viability was calculated to be 42.3 ± 1.4%. As a proof-of-concept, we determined these values to be acceptable, demonstrating that large quantities of cells can be encapsulated and printed using this temperature-dependent procedure while maintaining some viability. While the observed viabilities are low relative to current standards of the field, this is in some part due to using settings that have been optimized for acellular printability rather than cellular viability. Increasing the cartridge temperature, changing the nozzle size or ink concentration, and using a lower cell density are all possible changes that could be made to increase the cell viability, but a more rigorous investigation of these factors is outside the scope of the present work. Additionally, the maintenance of cell viability between the two timepoints suggests that TGM inks are effective at maintaining cellular viability once encapsulated, although this too would need to be verified in a future, longer study.

4. Conclusions

In this work, we present a novel bioprinting system utilizing a dual-gelling PNIPAAm-based bioink and a poloxamer support bath. We demonstrate that we can leverage the low viscosity and thermal gelation of the ink to print precisely placed fibers and construct multilayered scaffolds on a millimeter scale while maintaining high-resolution and uniformity, making this an effective tool for producing both acellular and cellular tissue engineering constructs with complex architectures. In doing so, we examined part of the web of relationships between printing factors that ultimately affect printing outcomes within this system. Thermogelling materials have not been utilized extensively in bioink design, partially due to difficulties with maintaining appropriate temperatures. However, these challenges can be overcome with innovations in hardware, such as cooled, mixing heads and insulated or actively cooled nozzles, and the results in this work demonstrate the benefits thermal gelation can provide towards bioprinting resolution. We also have taken a PNIPAAm-based material previously used with success as an injectable material for osteochondral tissue engineering and successfully adapted it to 3D printing, enabling a much broader range of architectural complexity for scaffolds made with this relatively

hydrophobic material. Synperonic® F-108 is an off-the-shelf compound that can be used to produce effective support baths that maintain delicate printed structures within a hydrated, heated environment, which is ideal for cell printing with various types of inks and is not solely limited to printing with TGM. On the whole, this work provides a bioprinting system consisting of a novel bioink and support bath, and an infrequently used dual-gelation mechanism, that leverages the characteristics of each to produce uniform multilayered hydrogel scaffolds with fibers under 200 μm in diameter.

CRediT authorship contribution statement

Adam M. Navara: Conceptualization, Methodology, Validation, Formal analysis, Investigation, Writing – original draft, Writing – review & editing, Visualization. **Yu Seon Kim:** Methodology, Writing – review & editing. **Yilan Xu:** Investigation, Writing – review & editing. **Christopher L. Crafton:** Investigation, Writing – review & editing. **Mani Diba:** Methodology, Writing – review & editing. **Jason L. Guo:** Methodology, Writing – review & editing. **Antonios G. Mikos:** Conceptualization, Methodology, Resources, Writing – review & editing, Supervision, Funding acquisition.

Declaration of competing interest

The authors have no conflicts of interest to disclose.

Acknowledgements

The authors would like to thank the National Institutes of Health (P41 EB023833) and the National Science Foundation Graduate Research Fellowship Program (A.M.N.) for financial support. M.D. was supported by a Rubicon postdoctoral fellowship from the Dutch Research Council (NWO; Project No. 019.182 EN.004). The authors would also like to thank Gerry Koons for assistance with APC and Letitia Chim for assistance with statistical analysis.

Appendix A. Supplementary data

Supplementary data to this article can be found online at https://doi.org/10.1016/j.bioactmat.2021.11.016.

References

[1] W. Sun, B. Starly, A.C. Daly, J.A. Burdick, J. Groll, G. Skeldon, W. Shu, Y. Sakai, M. Shinohara, M. Nishikawa, J. Jang, D.-W. Cho, M. Nie, S. Takeuchi, S. Ostrovidov, A. Khademhosseini, R.D. Kamm, V. Mironov, L. Moroni, I.T. Ozbolat, The bioprinting roadmap, Biofabrication 12 (2020), 022002, https://doi.org/10.1088/1758-5090/ab5158.

[2] D. Lei, Y. Yang, Z. Liu, B. Yang, W. Gong, S. Chen, S. Wang, L. Sun, B. Song, H. Xuan, X. Mo, B. Sun, S. Li, Q. Yang, S. Huang, S. Chen, Y. Ma, W. Liu, C. He, B. Zhu, E.M. Jeffries, F.-L. Qing, X. Ye, Q. Zhao, Z. You, 3D printing of biomimetic vasculature for tissue regeneration, Mater. Horiz. 6 (2019) 1197–1206, https://doi.org/10.1039/C9MH00174C.

[3] D. Lei, B. Luo, Y. Guo, D. Wang, H. Yang, S. Wang, H. Xuan, A. Shen, Y. Zhang, Z. Liu, C. He, F.-L. Qing, Y. Xu, G. Zhou, Z. You, 4-Axis printing microfibrous tubular scaffold and tracheal cartilage application, Sci. China Mater. 62 (2019) 1910–1920, https://doi.org/10.1007/s40843-019-9498-5.

[4] M.L. Bedell, A.M. Navara, Y. Du, S. Zhang, A.G. Mikos, Polymeric systems for bioprinting, Chem. Rev. 120 (2020) 10744–10792, https://doi.org/10.1021/acs.chemrev.9b00834.

[5] I. Donderwinkel, J.C.M. van Hest, N.R. Cameron, Bio-inks for 3D bioprinting: recent advances and future prospects, Polym. Chem. 8 (2017) 4451–4471, https://doi.org/10.1039/C7PY00826K.

[6] G. Decante, J.B. Costa, J. Silva-Correia, M.N. Collins, R.L. Reis, J.M. Oliveira, Engineering bioinks for 3D bioprinting, Biofabrication 13 (2021), 032001, https://doi.org/10.1088/1758-5090/abec2c.

[7] G.L. Koons, M. Diba, A.G. Mikos, Materials design for bone-tissue engineering, Nat. Rev. Mater. 5 (2020) 584–603, https://doi.org/10.1038/s41578-020-0204-2.

[8] I.T. Ozbolat, M. Hospodiuk, Current advances and future perspectives in extrusion-based bioprinting, Biomaterials 76 (2016) 321–343, https://doi.org/10.1016/j.biomaterials.2015.10.076.

[9] S. Ramesh, O.L.A. Harrysson, P.K. Rao, A. Tamayol, D.R. Cormier, Y. Zhang, I. V. Rivero, Extrusion bioprinting: recent progress, challenges, and future opportunities, Bioprinting 21 (2021), e00116, https://doi.org/10.1016/j.bprint.2020.e00116.

[10] N. Paxton, W. Smolan, T. Böck, F. Melchels, J. Groll, T. Jungst, Proposal to assess printability of bioinks for extrusion-based bioprinting and evaluation of rheological properties governing bioprintability, Biofabrication 9 (2017), 044107, https://doi.org/10.1088/1758-5090/aa8dd8.

[11] D. Wu, Y. Yu, J. Tan, L. Huang, B. Luo, L. Lu, C. Zhou, 3D bioprinting of gellan gum and poly (ethylene glycol) diacrylate based hydrogels to produce human-scale constructs with high-fidelity, Mater. Des. 160 (2018) 486–495, https://doi.org/10.1016/j.matdes.2018.09.040.

[12] Y. He, F. Yang, H. Zhao, Q. Gao, B. Xia, J. Fu, Research on the printability of hydrogels in 3D bioprinting, Sci. Rep. 6 (2016), https://doi.org/10.1038/srep29977.

[13] M.E. Cooke, D.H. Rosenzweig, The rheology of direct and suspended extrusion bioprinting, APL Bioeng 5 (2021), 011502, https://doi.org/10.1063/5.0031475.

[14] J. Gao, X. Ding, X. Yu, X. Chen, X. Zhang, S. Cui, J. Shi, J. Chen, L. Yu, S. Chen, J. Ding, Cell-free bilayered porous scaffolds for osteochondral regeneration fabricated by continuous 3D-printing using nascent physical hydrogel as ink, Adv. Healthc. Mater. 10 (2021) 2001404, https://doi.org/10.1002/adhm.202001404.

[15] M. Kesti, M. Müller, J. Becher, M. Schnabelrauch, M. D'Este, D. Eglin, M. Zenobi-Wong, A versatile bioink for three-dimensional printing of cellular scaffolds based on thermally and photo-triggered tandem gelation, Acta Biomater. 11 (2015) 162–172, https://doi.org/10.1016/j.actbio.2014.09.033.

[16] M. Janmaleki, J. Liu, M. Kamkar, M. Azarmanesh, U. Sundararaj, A.S. Nezhad, Role of temperature on bio-printability of gelatin methacryloyl bioink in two-step cross-linking strategy for tissue engineering applications, Biomed, Materials 16 (2020), 015021, https://doi.org/10.1088/1748-605X/abbcc9.

[17] W. Lim, G.J. Kim, H.W. Kim, J. Lee, X. Zhang, M.G. Kang, J.W. Seo, J.M. Cha, H. J. Park, M.-Y. Lee, S.R. Shin, S.Y. Shin, H. Bae, Kappa-carrageenan-based dual crosslinkable bioink for extrusion type bioprinting, Polymers 12 (2020) 2377, https://doi.org/10.3390/polym12102377.

[18] T.J. Hinton, Q. Jallerat, R.N. Palchesko, J.H. Park, M.S. Grodzicki, H.-J. Shue, M. H. Ramadan, A.R. Hudson, A.W. Feinberg, Three-dimensional printing of complex biological structures by freeform reversible embedding of suspended hydrogels, Sci. Adv. 1 (2015), e1500758, https://doi.org/10.1126/sciadv.1500758.

[19] T.J. Hinton, A. Hudson, K. Pusch, A. Lee, A.W. Feinberg, 3D printing PDMS elastomer in a hydrophilic support bath via freeform reversible embedding, ACS Biomater. Sci. Eng. 2 (2016) 1781–1786, https://doi.org/10.1021/acsbiomaterials.6b00170.

[20] A. Lee, A.R. Hudson, D.J. Shiwarski, J.W. Tashman, T.J. Hinton, S. Yerneni, J. M. Bliley, P.G. Campbell, A.W. Feinberg, 3D bioprinting of collagen to rebuild components of the human heart, Science 365 (2019) 482–487, https://doi.org/10.1126/science.aav9051.

[21] E. Mirdamadi, N. Muselimyan, P. Koti, H. Asfour, N. Sarvazyan, Agarose slurry as a support medium for bioprinting and culturing freestanding cell-laden hydrogel constructs, 3D Print. Addit. Manuf. 6 (2019) 158–164, https://doi.org/10.1089/3dp.2018.0175.

[22] A. Shapira, N. Noor, H. Oved, T. Dvir, Transparent support media for high resolution 3D printing of volumetric cell-containing ECM structures, Biomed. Mater. 15 (2020), 045018, https://doi.org/10.1088/1748-605X/ab809f.

[23] E.Y.S. Tan, R. Suntornnond, W.Y. Yeong, High-resolution novel indirect bioprinting of low-viscosity cell-laden hydrogels via model-support bioink interaction, 3D Print. Addit. Manuf. 8 (2021) 69–78, https://doi.org/10.1089/3dp.2020.0153.

[24] A.K. Ekenseair, K.W.M. Boere, S.N. Tzouanas, T.N. Vo, F.K. Kasper, A.G. Mikos, Synthesis and characterization of thermally and chemically gelling injectable hydrogels for tissue engineering, Biomacromolecules 13 (2012) 1908–1915, https://doi.org/10.1021/bm300429e.

[25] T.N. Vo, A.K. Ekenseair, F.K. Kasper, A.G. Mikos, Synthesis, physicochemical characterization, and cytocompatibility of bioresorbable, dual-gelling injectable hydrogels, Biomacromolecules 15 (2014) 132–142, https://doi.org/10.1021/bm401413c.

[26] J.L. Guo, Y.S. Kim, V.Y. Xie, B.T. Smith, E. Watson, J. Lam, H.A. Pearce, P.S. Engel, A.G. Mikos, Modular, tissue-specific, and biodegradable hydrogel cross-linkers for tissue engineering, Sci. Adv. 5 (2019), https://doi.org/10.1126/sciadv.aaw7396 eaaw7396.

[27] Y.S. Kim, J.L. Guo, J. Lam, K.J. Grande-Allen, P.S. Engel, A.G. Mikos, Synthesis of injectable, thermally responsive, chondroitin sulfate-cross-linked poly(N-isopropylacrylamide) Hydrogels, ACS Biomater. Sci. Eng. 5 (2019) 6405–6413, https://doi.org/10.1021/acsbiomaterials.9b01450.

[28] T.N. Vo, A.K. Ekenseair, P.P. Spicer, B.M. Watson, S.N. Tzouanas, T.T. Roh, A. G. Mikos, In vitro and in vivo evaluation of self-mineralization and biocompatibility of injectable, dual-gelling hydrogels for bone tissue engineering, J. Contr. Release 205 (2015) 25–34, https://doi.org/10.1016/j.jconrel.2014.11.028.

[29] L. Ouyang, R. Yao, Y. Zhao, W. Sun, Effect of bioink properties on printability and cell viability for 3D bioplotting of embryonic stem cells, Biofabrication 8 (2016), 035020, https://doi.org/10.1088/1758-5090/8/3/035020.

[30] J.F. Ryder, J.M. Yeomans, Shear thinning in dilute polymer solutions, J. Chem. Phys. 125 (2006) 194906, https://doi.org/10.1063/1.2387948.

[31] A. Forget, A. Blaeser, F. Miessmer, M. Köpf, D.F.D. Campos, N.H. Voelcker, A. Blencowe, H. Fischer, V.P. Shastri, Mechanically tunable bioink for 3D bioprinting of human cells, Adv. Healthc. Mater. 6 (2017) 1700255, https://doi.org/10.1002/adhm.201700255.

[32] B.L. Ekerdt, C.M. Fuentes, Y. Lei, M.M. Adil, A. Ramasubramanian, R.A. Segalman, D.V. Schaffer, Thermoreversible hyaluronic acid-PNIPAAm hydrogel systems for

3D stem cell culture, Adv. Healthc. Mater. 7 (2018) 1800225, https://doi.org/10.1002/adhm.201800225.

[33] T. Lorson, S. Jaksch, M.M. Lübtow, T. Jüngst, J. Groll, T. Lühmann, R. Luxenhofer, A Thermogelling supramolecular hydrogel with sponge-like morphology as a cytocompatible bioink, Biomacromolecules 18 (2017) 2161–2171, https://doi.org/10.1021/acs.biomac.7b00481.

[34] Q.L. Loh, C. Choong, Three-dimensional scaffolds for tissue engineering applications: role of porosity and pore size, Tissue Eng. B Rev. 19 (2013) 485–502, https://doi.org/10.1089/ten.teb.2012.0437.